

Tailoring nanostructured surfaces with plasmonic/magnetic multifunctional response

A. Serrano, O. Rodríguez de la Fuente, M. García-Hernández, G. Campo, C. de Julián Fernández, J. F. Fernández, and M. A. García

Citation: *Appl. Phys. Lett.* **113**, 101908 (2018); doi: 10.1063/1.5044697

View online: <https://doi.org/10.1063/1.5044697>

View Table of Contents: <http://aip.scitation.org/toc/apl/113/10>

Published by the American Institute of Physics

Articles you may be interested in

[Stretchable IR metamaterial with ultra-narrowband perfect absorption](#)

Applied Physics Letters **113**, 101907 (2018); 10.1063/1.5044225

[Antireflection-assisted all-dielectric terahertz metamaterial polarization converter](#)

Applied Physics Letters **113**, 101104 (2018); 10.1063/1.5042784

[Frequency-dependent transmission-type digital coding metasurface controlled by light intensity](#)

Applied Physics Letters **113**, 091601 (2018); 10.1063/1.5045718

[Resonant metasurface with tunable asymmetric reflection](#)

Applied Physics Letters **113**, 094103 (2018); 10.1063/1.5046948

[Merging bands of polarization converters by suppressing Fano resonance](#)

Applied Physics Letters **113**, 101901 (2018); 10.1063/1.5048247

[Heavily overdamped resonance structurally engineered in a grating metasurface for ultra-broadband acoustic absorption](#)

Applied Physics Letters **113**, 101903 (2018); 10.1063/1.5047798

AIP | Conference Proceedings

**Get 30% off all
print proceedings!**

Enter Promotion Code **PDF30** at checkout



Tailoring nanostructured surfaces with plasmonic/magnetic multifunctional response

A. Serrano,^{1,2,a)} O. Rodríguez de la Fuente,^{2,3} M. García-Hernández,⁴ G. Campo,^{5,6}
 C. de Julián Fernández,^{6,7} J. F. Fernández,¹ and M. A. García^{1,3}

¹*Instituto de Cerámica y Vidrio, ICV-CSIC, C/Kelsen 5, Cantoblanco, 28049 Madrid, Spain*

²*Departamento de Física de Materiales, Universidad Complutense de Madrid, Avda. Complutense s/n, 28040 Madrid, Spain*

³*Instituto de Magnetismo Aplicado “Salvador Velayos,” Universidad Complutense de Madrid, 28230 Madrid, Spain*

⁴*Instituto de Ciencia de Materiales, ICMM-CSIC, C/Sor Juana Inés de la Cruz 3, Cantoblanco, 28049 Madrid, Spain*

⁵*CNR-INO and European Laboratory for Nonlinear Spectroscopy (LENS), via Carrara 1, 50019 Sesto Fiorentino, Italy*

⁶*INSTM and Dipartimento di Chimica “U. Schiff,” Università degli Studi di Firenze, via della Lastruccia 3, I-50019 Sesto Fiorentino, Italy*

⁷*INEM-CNR, Parco Area delle Scienze 37/A, I-43124 Parma, Italy*

(Received 15 June 2018; accepted 19 August 2018; published online 7 September 2018)

In this work, we present an innovative way to functionalize large surfaces combining both plasmonic and magnetic nanoparticles on a substrate, by the growth of bilayers and a subsequent single annealing. In particular, we show here the formation of Au and γ -Fe₂O₃ nanoparticles using this route. Thermal treatments promote the nanostructuration of the film plus a partial oxidation of Fe to form ferrimagnetic oxides. For this purpose, annealing conditions and the structure of the bilayer must be selected to achieve an optimal nanostructuration, avoiding the full oxidation of Fe to form antiferromagnetic hematite. *Published by AIP Publishing.*

<https://doi.org/10.1063/1.5044697>

Functionalization of surfaces with nanoparticles (NPs) allows tuning their properties to optimize them for specific applications.^{1–8} For instance, surface functionalization with noble metal NPs permits the excitation of localized surface plasmons that may enhance photocatalytic activity, biomarkers sensitivity, or light absorption. Similarly, functionalization with transition metal oxide (TMO) nanostructures is used to induce magnetic properties, enhanced reactivity, and mechanical resistance or to tune local heating. In addition, hybrid functionalization of surfaces metal and TMO provides further advantages. Specifically, complex NPs, such as core-shell, nano-agglomerates, or nano-dimers, present an added interest since they can exhibit further advantages combining the properties of their individual components with other emerging properties arising from their interaction because of interface and proximity effects.^{9,10} For instance, the coexistence of plasmonic and TMO NPs improves the photocatalytic activity.^{11,12} In particular, hematite (α -Fe₂O₃) and Au nanostructures largely enhance the photocatalytic response of CO oxidation and the efficiency for solar water splitting with respect to that observed when just α -Fe₂O₃ nanostructures are present.^{13,14}

In a recent paper, we proposed a new method to functionalize surfaces with both noble metal and TMO nanostructures.¹⁵ This route consists in the deposition of bilayers plus a subsequent annealing. We demonstrated that this method was useful to functionalize large areas with Au/ α -Fe₂O₃ NPs. Upon annealing in air, the difference in the

thermal expansion coefficient between the glass and the Au film induces interfacial thermal stresses that are relieved upon the formation of hillocks. At temperatures large enough, holes are formed and grow, percolating and leading to the formation of Au islands that become rounded in order to reduce surface energy.¹⁶ In the case of transition metals, the oxidation upon annealing in air induces an increase in volume ($\sim 30\%$ – 40%) that yields stresses which are also relieved upon film nanostructuration.¹⁷ Hence, annealing of bilayers leads to the formation of both noble metal and TMO nanostructures co-existing on the same substrate by a mixture of the abovementioned processes. Additionally, the morphology of the nanostructures could be controlled through the deposition and annealing parameters. Therefore, this growth mechanism can be considered as a route to obtain hybrid nanostructures for several applications. Obtaining other iron oxide phases such as Fe₃O₄ and γ -Fe₂O₃ NPs, instead α -Fe₂O₃, in combination with the Au NPs can be appealing due to their magnetic properties.¹⁸ However, the main limitation of this technique is the large temperature required to achieve the nanostructuration of the bilayer ($\sim 1000^\circ\text{C}$), which induces the full oxidation of Fe to form α -Fe₂O₃, that is weak ferromagnetic. Annealing in vacuum is not a straightforward solution. In the solid-state dewetting process, which leads to nanostructuration of noble metal films, the mechanism for mass transport is surface diffusion. The surface diffusion coefficient (SDC) increases several orders of magnitude upon annealing in the oxygen-rich atmosphere,¹⁹ so annealing in vacuum leads to weak nanostructuration instead of rounded and well-separated NPs. The SDC can be enhanced by increasing the annealing temperature, but above 1063°C , Au films melt and tend to detach and sublime from the substrate.

^{a)}Author to whom correspondence should be addressed: aida.serrano@icv.csic.es

In this complex situation, we explore in this work if there is a set of parameters which allows obtaining the combination of plasmonic noble metal/ferrimagnetic oxides NPs over large areas with the deposition plus annealing route, i.e., exploiting the solid-state dewetting process. In particular, we investigate the formation of nanostructures by annealing in low vacuum (to reduce moderately the SDC) and at a temperature slightly above the Au melting temperature (i.e., 1100 °C, to partially compensate the reduction of SDC). Also, we place the Fe layer on top of the Au film, to prevent Au sublimation but still allowing the formation of Au NPs. We find a window of parameters that permits obtaining, in a single process, large surfaces exhibiting both plasmonic and magnetic properties at room temperature (RT). The morphology of the NPs can be tuned by varying the initial parameters, such as the film thickness, and the industrial scalability of the growth technique is doable.

Samples were prepared from the deposition of Au/Fe bilayers and a subsequent annealing in low vacuum. Thin films were grown on silica substrates by thermal evaporation using a tungsten filament and Au and Fe wires as the source in a home-made evaporation chamber. The vacuum in the chamber during the film deposition was 10^{-6} Torr, and the deposition rate was of 0.02 nm/s, controlled with a Q-microbalance previously calibrated with X-ray reflectometry. The distance between the filament and the substrates was about 20 cm. The area of the substrate that was coated with the metallic films was about $2 \times 2 \text{ cm}^2$. Prior to deposition, the substrate surface was cleaned with soap, rinsed with deionized water, and dried with dry air. Thermal treatments were carried out in a quartz tube furnace in low vacuum conditions (10^{-2} – 10^{-3} Torr) for 12 h at 1100 °C.

The morphology of the samples was studied by scanning electron microscopy (SEM) using a TM-1000 Hitachi Tabletop Microscope, with an accelerating voltage of 15 kV. Atomic force microscopy (AFM) images were obtained with a Nanotec instrument and measurements were performed in air, using silicon tips (with a resonant frequency of 200–300 kHz), in the non-contact mode at RT. The images were analyzed using the $\text{WS} \times \text{M}^{20}$ software package from Nanotec. Confocal Raman microscopy (CRM) of samples was carried out using a Witec ALPHA 300RA. Measurements were performed with a linearly polarized Nd:YAG laser (532 nm). The optical resolution of the confocal microscope is 200 nm and 500 nm in the lateral and vertical directions, respectively. In this work, Raman spectra were recorded at RT each 100 nm in the spectral range of 0 – 3600 cm^{-1} . In order to avoid any damage in the samples, laser excitation power was fixed at 0.7 mW. Raman measurements were performed using an objective with a lens of numerical aperture, NA, of 0.95. Collected spectra were analyzed using the Witec Control Plus Software. Optical absorption spectra of the samples were recorded using a V-670 UV-Visible double beam spectrophotometer in the transmission mode at RT. The absorption signal was referenced to a silica substrate in order to obtain the net optical absorption of samples. The magnetic characterization of the samples was carried out using a superconducting quantum interference device (SQUID) from Quantum Design. The magnetic circular dichroism (MCD) spectra and hysteresis loops were acquired using a home-built setup described in Ref. 21 in

the spectral interval between 300 and 1000 nm and applying a maximum magnetic field of 13 kOe perpendicularly to the surface plane of samples.

Figure 1 shows the SEM micrographs for two samples fabricated from a Au/Fe bilayer annealed at 1100 °C for 12 h at a nominal pressure of 3×10^{-2} Torr. The Au film thickness is 10 nm for both samples, while the Fe film thickness is 5 and 10 nm, respectively. Samples exhibit nanostructures of the order of hundreds of nanometres along the whole surface. The existence of regions with different nanostructure sizes should be noted. The presence of irregularities at the films, at the substrate, and/or at the film/substrate interfaces favours the presence of inhomogeneous stresses which induce the breaking of the layers during the annealing. Finally, the fragments of the Fe and Au layers having high chemical potential produce pseudo-spherical NPs. The influence of the Fe film thickness is already apparent, and an increase in a clear bimodal distribution in the NP size appears as the film thickness is increased. The sample obtained from a 10 nm Au/5 nm Fe bilayer [Fig. 1(a)] shows NPs with an average size in the range of 20–300 nm, while that obtained from a 10 nm Au/10 nm Fe bilayer [Fig. 1(b)] presents nanostructures with a set of NPs with their size ranging between 50 and 150 nm plus some other NPs with sizes of the order of 0.5–1 μm , showing an average height similar in both kinds of NPs [around 10–40 nm, as shown in Figs. 1(c) and 1(d)]. The presence of large nanostructures with flat faces is thermodynamically driven by the Ostwald ripening process because large particles are more energetically favorable than smaller particles.²² This process is more pronounced in certain regions of the surface. In fact, the thicker sample of the Fe layer presents an irregular pattern with regions having smaller particles and regions where particles have grown. Therefore, by fixing the Au film thickness and varying the Fe film thickness, it is possible to tune the morphological

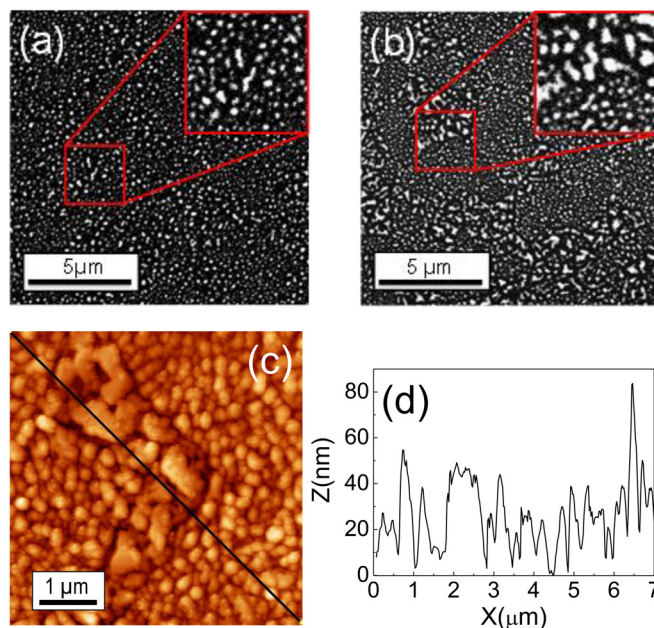


FIG. 1. SEM image for a (a) 10 nm Au/5 nm Fe and (b) 10 nm Au/10 nm Fe bilayer annealed at 1100 °C for 12 h at a nominal pressure of 3×10^{-2} Torr. (c) Topography AFM image for the 10 nm Au/10 nm Fe bilayer annealed and (d) height profile measured along the line indicated in the AFM image.

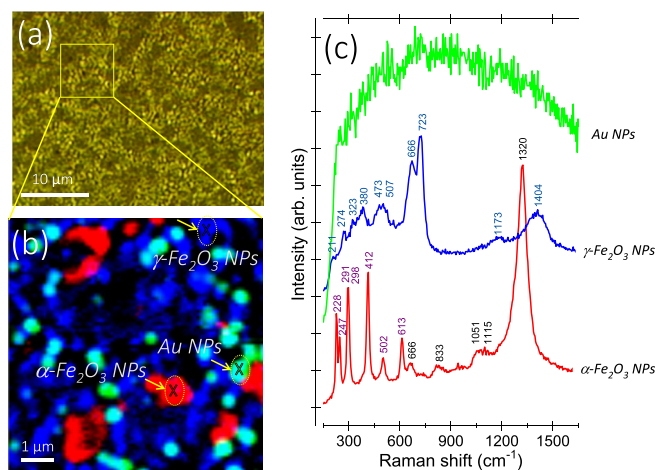


FIG. 2. (a) Optical image of a 10 nm Au/10 nm Fe bilayer annealed at 1100 °C for 12 h at a nominal pressure of 3×10^{-2} Torr. (b) False colour image of compositional mapping showing the presence of Au (green), maghemite (blue), and hematite (red) nanostructures. The Raman intensity image is obtained from mapping the area marked with a yellow square on the optical image (a) and collected single Raman spectra taken each 100 nm, integrating in the spectral range from 690 to 780 cm⁻¹ for γ-Fe₂O₃, from 1220 to 1390 cm⁻¹ for α-Fe₂O₃, and from 70 to 3600 cm⁻¹ for the Au nanostructures. (c) Single Raman spectra taken from the corresponding crosses marked in the Raman image (b). Raman bands of α-Fe₂O₃ and γ-Fe₂O₃ are identified.

features of the final nanostructures. The morphological distribution of NPs fabricated from single Fe films (without Au) is similar to that obtained for Au/iron oxide nanostructures (see [supplementary material](#)).

Samples were analysed by CRM in order to examine the distribution of both Au and iron oxide nanostructures and to determine the oxidation state of iron oxide. In this study, we discriminate three different types of Raman spectra corresponding to the presence of Au (green), γ-Fe₂O₃ (blue), and α-Fe₂O₃ (red) nanostructures, as summarized in Fig. 2. The CRM analysis obtained from the 10 nm Au/10 nm Fe bilayer annealed at 1100 °C for 12 h points out that large particles are hematite while the small ones are maghemite and Au NPs. This fact could be related to a coalescence of iron oxide to form large particles in certain regions. As the formation of large nanostructures is attained to minimize the system energy, the iron oxide large particles stabilize in the hematite polymorph.

A quantitative analysis by CRM, obtained from several regions at the surface, indicates that about 80% of iron oxide

corresponds to maghemite while the rest is hematite. A similar proportion of iron oxide phases is measured for the sample stemming from the annealing of a thinner 5 nm Fe sample. An additional study (see [supplementary material](#)) of 10 nm Fe films (without Au) annealed under the same conditions shows a larger proportion of maghemite (99%) than for the case of annealed Au/Fe bilayers, indicating that Au assists in the Fe to α-Fe₂O₃ transformation. The irregular pattern induced by the Au film and its nanostructuration during the annealing favours the phase transition γ-Fe₂O₃ → α-Fe₂O₃, in regions where the Au NPs are absent. Besides, it should be noted that, despite Au NPs are homogeneously distributed throughout the substrate, a larger fraction is close to the maghemite NPs (around 80%), limiting the growth of iron oxide nanostructures.

Figure 2(c) presents single Raman spectra taken from the surface Raman intensity image on the marked crosses. The fluorescence signal is assigned to Au NPs. α-Fe₂O₃ NPs show the seven phonon modes (2A_{1g} + 5E_g) allowed in Raman²³ plus other Raman peaks that do not belong to the spatial group but that have been already reported in the literature.^{24–29} For γ-Fe₂O₃, besides the five allowed phonon modes, corresponding to A_{1g} + E_g + 3T_{2g}, other Raman bands related to the breaking of symmetry due to deviations at the stoichiometry can be also observed.^{30,31} A detailed analysis of the identified Raman modes is presented in the [supplementary material](#).

Figure 3(a) shows the optical absorption spectrum for a Au/Fe bilayer annealed for 12 h at 1100 °C in low vacuum (nominally 3×10^{-2} Torr). An absorption band located at 542 nm is clearly observed. This band is due to the excitation of surface plasmon resonance (SPR) in Au NPs.^{32,33} A numerical analysis of the spectrum points out that the full-width-half maximum (FWHM) of the band is about 0.22 eV, which would correspond to spherical NPs of about 20–30 nm diameter.³⁴ However, it is well known that a wide distribution of NPs' size and shape led to wider absorption bands. Hence, our experimental optical absorption measurement corresponds to an average of Au NPs with a size distribution. Summing those non-centred absorption bands from different NPs, a wider band corresponds to individual NPs in the range of 50–150 nm (that would present FWHM below 0.05 eV). In addition, the position of this absorption band (542 nm) is that expected for Au NPs in a dielectric medium with $\epsilon \cong 2.25$, that is an intermediate value between the dielectric

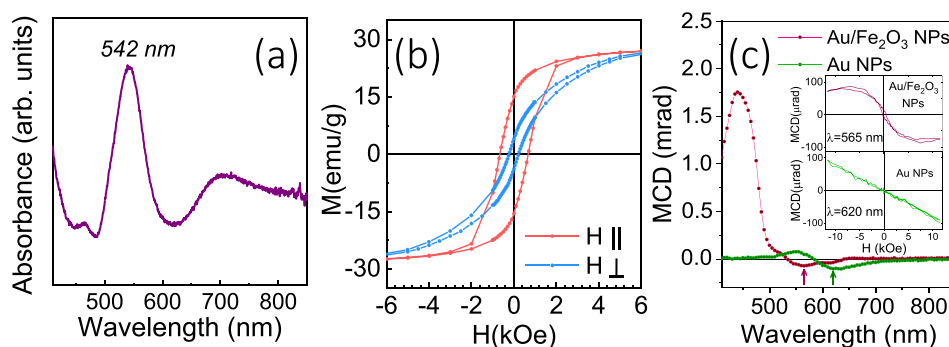


FIG. 3. (a) Optical absorption spectrum of a 10 nm Au/10 nm Fe bilayer annealed at 1100 °C for 12 h at a pressure of 3×10^{-2} Torr, exhibiting the absorption band of localized SPR from Au NPs. (b) Parallel and perpendicular magnetization curves at 300 K. The diamagnetic contribution from the substrate has been removed for the sake of clarity. (c) MCD spectrum of the Au/Fe₂O₃ system compared with that obtained for pure Au NPs prepared from a 10 nm Au thin film annealed at 400 °C in air. The inset of (c) presents the MCD loops recorded at 565 nm for Au/Fe₂O₃ NPs and at 620 nm for Au NPs.

permittivity of air and that of iron oxide, shifting the SPR band towards larger wavelengths than for single Au NPs in air. Besides, a smaller band is observed in the spectrum at about 730 nm. This band may originate from elongated NPs and corresponds to longitudinal SPs. Actually, the above described structural characterization showed some elongated nanostructures with an aspect ratio around 2.5–3, which would correspond to the longitudinal SPR falling at about 700–760 nm,³² as that observed here.

The magnetization curves at 300 K with the field in the parallel and perpendicular directions to the sample surface are shown in Fig. 3(b). For both configurations, the curves exhibit a hysteresis loop characteristic of ferro/ferrimagnetic materials. Similar results were found at 4 K (see [supplementary material](#)). The saturation magnetization (M_s) is close to 30 emu/g and very similar at 4 K and 300 K, which is in agreement with the co-existence of maghemite that is ferrimagnetic ($M_s \sim 74$ –80 emu/g) and hematite that is antiferromagnetic at low temperature exhibiting weak ferromagnetism above the Morin transition (250 K) with $M_s \sim 1$ emu/g.¹⁸ Larger values of M_s (60–70 emu/g) were obtained for γ -Fe₂O₃ NPs prepared from a 10 nm Fe film annealed under the same conditions, which are closer to that of the bulk maghemite (see [supplementary material](#)). The coercive field of the magnetization curves at 300 K is about 700 Oe and 220 Oe while the remanence is 60% and 20% of M_s with the field in parallel and perpendicular configurations, respectively. The different shapes of magnetization curves measured with the in-plane and out-of-plane fields to the sample surface can be understood in terms of shape anisotropy. According to micrographs in Fig. 1, Fe₂O₃ NPs exhibit an aspect ratio of ~ 10 leading to a demagnetization factor of 0.8 and 0.1 out-of-plane and in-plane, respectively. The shape anisotropy for Fe₂O₃ is then $[\sim 1/2\mu_0 \cdot M_s^2(N_z - N_{xy})]$ of the order of 100 kJ/m³, while the magnetocrystalline anisotropy is about 5 kJ/m³,³⁵ and consequently, the easy axis of magnetization is along the nanostructure plane.

In order to analyze the effect of the combination of Au and Fe₂O₃ nanostructures, magneto-optical MCD measurements were carried out for a Au/Fe bilayer annealed for 12 h at 1100 °C h at a nominal pressure of 3×10^{-2} Torr, and a simple Au nanostructured system prepared by a similar dewetting procedure, as is shown in Fig. 3(c). Au nanostructures were prepared following the same growth procedure from Au thin films of 10 nm thickness annealed at 400 °C in air according to Ref. 16. The MCD spectrum of the Au and iron oxide nanostructures corresponds to that expected in maghemite one,²¹ while Au NPs exhibit a typical derivative-like MCD curve similar to other studies.³⁶ The inset of Fig. 3(c) shows the MCD hysteresis loops nearby the respective SPR for Au and Fe₂O₃ nanostructures, whereas for single Au nanostructures, the magneto-optical signal is presented at a wavelength out of the SPR peak since the MCD signal crosses zero at the resonance.³⁶ The MCD signal for Au NPs at 620 nm follows a linear dependence with the magnetic field, characteristic of these NPs,³⁶ while the Au/Fe₂O₃ system presents a hysteresis loop characteristic of a ferro/ferrimagnetic material. Hence, in this complex system, we can find simultaneously the optical fingerprint of its plasmonic

and magnetic features by optical recording the absorption or the magnetic dichroism.

In conclusion, we have shown here that deposition of Fe/Au bilayers plus subsequent annealing in a controlled atmosphere (low vacuum conditions) can be used to functionalize large surfaces with Au/ γ -Fe₂O₃ NPs (with maghemite as the majority iron oxide phase) exhibiting both plasmonic and magnetic properties at RT, thus providing multifunctional surfaces. For this purpose, there is a window of annealing parameters (annealing temperature ~ 1100 °C, vacuum 10^{-2} – 10^{-3} Torr) and a particular structure (Fe top layer) that allows the tailored synthesis of both components.

See [supplementary material](#) for morphological characterization, confocal Raman microscopy, and magnetic measurements of iron oxide nanostructures obtained from Fe films annealed in vacuum and Raman spectroscopy analysis and magnetic measurements of Au and iron oxide nanostructures obtained from Au/Fe films annealed in vacuum.

This project was supported by a 2016 BBVA Foundation Grant for Researchers and Cultural Creators. This work was also supported by the Ministerio Español de Economía y Competitividad (MINECO) through Project Nos. MAT2017-86540-C4-1-R, MAT2014-52405-C02-02, and CSIC 20150E068. A.S. acknowledges the Comunidad de Madrid for the financial support (Grant No. 2017-t2/IND-5395).

The authors declare no competing financial interest.

- ¹S. Aggarwal, A. P. Monga, S. R. Perusse, R. Ramesh, V. Ballarotto, E. D. Williams, B. R. Chalamala, Y. Wei, and R. H. Reuss, *Science* **287**(80), 2235 (2000).
- ²R. R. S. R. Shinde, A. S. Ogale, S. B. Ogale, S. Aggarwal, V. Novikov, and E. D. Williams, *Phys. Rev. B* **64**, 35408 (2001).
- ³A. N. Shipway and I. Willner, *Chem. Commun.* **20**, 2035 (2001).
- ⁴I. W. Shipway and E. Katz, *ChemPhysChem* **1**, 18 (2000).
- ⁵P. Matheu, S. H. Lim, D. Derkacs, C. McPheeters, and E. T. Yu, *Appl. Phys. Lett.* **93**, 113108 (2008).
- ⁶S. L. Westcott, S. J. Oldenburg, T. R. Lee, and N. J. Halas, *Langmuir* **14**, 5396 (1998).
- ⁷S. P. Sundararajan, N. K. Grady, N. Mirin, and N. J. Halas, *Nano Lett.* **8**, 624 (2008).
- ⁸S. Pillai, K. R. Catchpole, T. Trupke, and M. A. Green, *J. Appl. Phys.* **101**, 093105 (2007).
- ⁹Y. Lee, M. A. Garcia, N. A. F. Huls, and S. Sun, *Angew. Chem., Int. Ed.* **49**, 1271 (2010).
- ¹⁰W. Wu, Q. He, and C. Jiang, *Nanoscale Res. Lett.* **3**, 397 (2008).
- ¹¹M. Xiao, R. Jiang, F. Wang, C. Fang, J. Wang, and J. C. Yub, *J. Mater. Chem. A* **1**, 5790 (2013).
- ¹²W. Hou and S. B. Cronin, *Adv. Funct. Mater.* **23**, 1612 (2013).
- ¹³L. Wang, H. Hu, N. T. Nguyen, Y. Zhang, P. Schmuki, and Y. Bi, *Nano Energy* **35**, 171 (2017).
- ¹⁴H. Gao, C. Liu, H. E. Jeong, and P. Yang, *ACS Nano* **6**, 234 (2012).
- ¹⁵A. Serrano, J. F. Fernandez, O. R. de la Fuente, and M. A. García, *Mater. Today Chem.* **4**, 64 (2017).
- ¹⁶A. Serrano, O. R. de la Fuente, and M. A. García, *J. Appl. Phys.* **108**, 74303 (2010).
- ¹⁷O. Kovalenko, J. R. Greer, and E. Rabkin, *Acta Mater.* **61**, 3148 (2013).
- ¹⁸R. M. Cornell and U. Schwertmann, *The Iron Oxides: Structure, Properties, Reactions, Occurrence and Uses*, 2nd ed. (Wiley-VCH Verlag GmbH & Co. KGaA, Weinheim, 2003).
- ¹⁹G. E. Rhead, *Acta Metall.* **13**, 223 (1965).
- ²⁰I. Horcas, R. Fernandez, J. M. Gomez-Rodriguez, J. Colchero, J. Gomez-Herrero, and A. M. Baro, *Rev. Sci. Instrum.* **78**, 013705 (2007).

- ²¹G. Campo, F. Pineider, V. Bonanni, M. Albino, A. Caneschi, C. Innocenti, C. de Julian Fernandez, and C. Sangregorio, *Chem. Mater.* **27**, 466–473 (2015).
- ²²L. Ratke and W. V. Peter, *Growth and Coarsening: Ostwald Ripening in Material Processing* (Springer Science & Business Media, 2002).
- ²³D. L. A. De Faria and S. Vena, *J. Raman Spectrosc.* **28**, 873 (1997).
- ²⁴K. F. McCarty, *Solid State Commun.* **68**, 799 (1988).
- ²⁵I. Cesar, K. Sivula, A. Kay, R. Zboril, and M. Gratzel, *J. Phys. Chem. C* **113**, 772 (2009).
- ²⁶T. P. Martin, R. Merlin, D. R. Huffman, and M. Cardona, *Solid State Commun.* **22**, 565 (1977).
- ²⁷F. J. Owens and J. Orosz, *Solid State Commun.* **138**, 95 (2006).
- ²⁸M. Lübke, A. M. Gigler, R. W. Stark, and W. Moritz, *Surf. Sci.* **604**, 679 (2010).
- ²⁹I. V. Chernyshova, M. F. Hochella, and A. S. Madden, *Phys. Chem. Chem. Phys.* **9**, 1736 (2007).
- ³⁰N. Boucherit, A. H.-L. Goff, and S. Joiret, *Corros. Sci.* **32**, 497 (1991).
- ³¹A. Demoulin, C. Trigance, D. Neff, E. Foy, P. Dillmann, and V. L. Hostis, *Corros. Sci.* **52**, 3168 (2010).
- ³²M. A. Garcia, *J. Phys. D: Appl. Phys.* **44**, 283001 (2011).
- ³³A. Serrano, *Modified Au-Based Nanomaterials Studied by Surface Plasmon Resonance Spectroscopy*, Springer Theses (Springer, 2015).
- ³⁴U. Kreibig and M. Vollmer, *Optical Properties of Metal Clusters*, Springer Series in Material Science (Springer-Verlag, Berlin, 1995).
- ³⁵J. M. D. Coey, *Magnetism and Magnetic Materials* (Cambridge University Press, 2010).
- ³⁶F. Pineider, G. Campo, V. Bonanni, C. de Julian Fernandez, G. Mattei, A. Caneschi, D. Gatteschi, and C. Sangregorio, *Nano Lett.* **13**, 4785–4789 (2013).